Bulletin of the Seismological Society of America, Vol. 108, No. 1, pp. 84–100, February 2018, doi: 10.1785/0120170070

Ⓔ

Documentation of Seven Earthquakes over the Past ~7000 Years on the West-Central Denali Fault at the Nenana River, Alaska

by J. Kade Carlson, Sean P. Bemis,* Nathan Toke, Bradley Bishop, and T. Patrick Taylor

Abstract The Denali fault in south-central Alaska is a major right-lateral strike-slip fault that parallels the Alaska Range for much of its length and represents the largest seismogenic source for interior Alaska. The fault system is over 1200 km in length, and identification of paleoseismic sites that preserve more than 2–3 paleoearthquakes has proven challenging due to its remote location and difficulty of access. In 2012 and 2015, we developed the Dead Mouse site, which provides the first long paleoearthquake record west of the 2002 M_w 7.9 Denali fault earthquake sequence rupture extent. This site is located on the west-central segment of the Denali fault near the southernmost intersection of the Parks Highway and the Nenana River. We hand-excavated three fault-perpendicular trenches and documented new evidence for seven surface-rupturing paleoearthquakes from deformation in the upper 2.5 m of stratigraphy. Evidence for these events includes offset units, filled fissures, upward fault terminations, and an angular unconformity. Chronological constraints from Bayesian sequence modeling of radiocarbon ages and one tentative tephra correlation indicate these seven earthquakes occurred at 388 cal B.P. (442–319; E1), 807 cal B.P. (853–764; E2), 1282 cal B.P. (1392–1160; E3), 2652 cal B.P. (2805–2460; E4), 3402 cal B.P. (3790–3010; E5*), 5673 cal B.P. (6676–4632; E6*), and 6987 cal B.P. (7281–6668; E7*). Although there are likely missing earthquakes in our chronology prior to E4, the intervals between E1 and E4 suggest significant variability in recurrence period at the Dead Mouse site. Additional paleoearthquake chronologies at neighboring sites are required to make reliable estimates of the spatial and temporal rupture history for the west-central Denali fault, but our data demonstrate the potential for recurrence periods as short as 300–600 yrs, well within range of the current open interval for the Denali fault at the Nenana River.

Electronic Supplement: Unannotated photomosaics, graphical output of our OxCal sequence model, OxCal sequence code, and table of depth-to-sand/gravel measurements.

Introduction

On 3 November 2002, an M_w 7.9 earthquake sequence ruptured 341 km of the Denali fault (Fig. 1) producing the largest strike-slip earthquake in North America in almost 150 yrs (Eberhart-Phillips *et al.*, 2003). At the time, this was the only known historic, or otherwise, surface-rupturing earthquake on the Denali fault. This event initiated an increased interest in, and highlighted the lack of, knowledge concerning seismic hazards present in south-central Alaska. Following the 2002 earthquake, the Denali fault has been a target of paleoseismic investigations and represents the largest seismogenic source for interior Alaska (Wesson *et al.*, 2007). During the summers of 2012 and 2015, we developed a new paleoseismic site, the Dead Mouse site, located on the west-central segment of the Denali fault near the southernmost intersection of the George Parks Highway and the Nenana River (63.45285° N, 148.80249° W; Fig. 1). The Dead Mouse site is located ~70 km from the western end of the 2002 Denali fault earthquake sequence surface-rupture terminus and ~45 km west of the M_w 6.7 Nenana Mountain foreshock epicenter (Fig. 1). The site is the most accessible paleoseismic site on the entire Denali fault system, as it is situated about 400 m from the highway (800 m by trail)

*Now at Global Forum on Urban and Regional Resilience, Virginia Polytechnic Institute and State University, 250 South Main Street, Suite 312, Blacksburg, Virginia 24060.

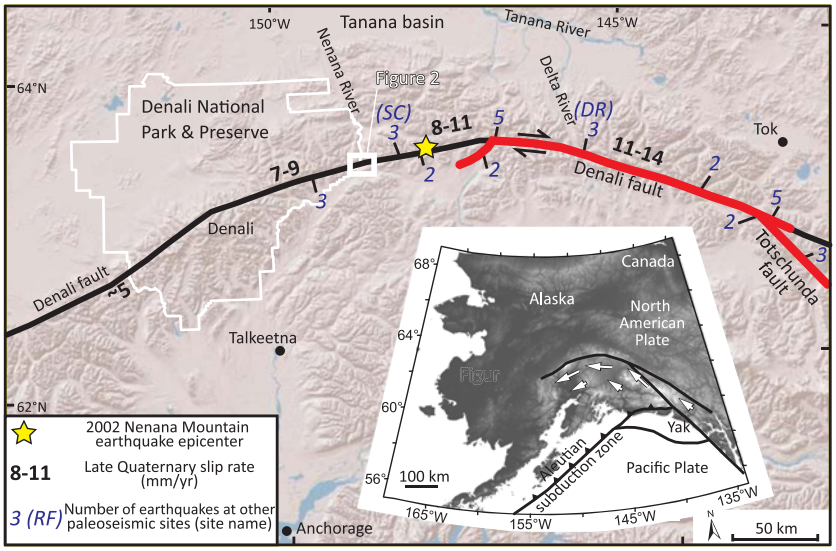

Figure 1. Regional topography, geographic features, and orogen-scale structures of the Alaska Range–Denali fault system (Plafker *et al.*, 1994; Koehler *et al.*, 2012). Late Quaternary slip rates are generalized from Matmon *et al.* (2006), Mériaux *et al.* (2009), and Haeussler *et al.* (2012). Other paleoseismic sites noted in the Discussion section: DR, Delta River (Plafker *et al.*, 2006); SC, Schist Creek (Personius *et al.*, 2015). Additional paleoseismic site information from Koehler *et al.* (2011), Schwartz *et al.* (2005, 2012), and Seitz *et al.* (2008). The inset map depicts the major active tectonic elements for south-central Alaska with arrows depicting plate motions relative to stable North America (modified from Freymueller *et al.*, 2008). Yak is the unsubducted portion of the Yakutat microplate. The thicker portion of the Denali fault delineates the 3 November 2002 M_w 7.9 rupture extent. Shaded-relief base from ESRI's ArcOnline resources and the elevation base for the inset map is derived from the U.S. Geological Survey GTOPO30 dataset (see Data and Resources). The color version of this figure is available only in the electronic edition.

and provides the only paleoseismic study directly within the Parks Highway infrastructural corridor.

The Denali fault is a major right-lateral intracontinental crustal strike-slip fault that closely parallels the Alaska Range as it spans much of south-central Alaska from east to west (Fig. 1). The fault and the elevated topography of the Alaska Range occur as far-field deformation from the collision and oblique flat-slab subduction of the Yakutat Block along the Pacific–North America plate boundary in southern Alaska (Eberhart-Phillips *et al.*, 2006; Haeussler, 2008). This far-field deformation extends into the interior of south-central Alaska and is accommodated through dextral slip on the Denali fault system (Haeussler, 2008; Bemis *et al.*, 2015). Dextral displacement initially developed along what is argued to be a structurally weak suture zone (e.g., Ridgway *et al.*, 2002) and has a post-Cretaceous dextral displacement west of Denali estimated to be ~140 km (Miller *et al.*, 2002) and late Cretaceous to early Tertiary displacement of about 400 km on the eastern section of the fault (Grantz, 1966; Nokleberg *et al.*, 1985; Hickman *et al.*, 1990; Plafker and Berg, 1994). Additionally, the Denali fault has the greatest slip rate of all nonplate boundary active faults for Alaska. Late Quaternary slip rates range from ~7 to 14 mm/yr with a clear pattern of westward decrease in velocity to the west of the Totschunda fault intersection (Matmon *et al.*, 2006; Mériaux *et al.*, 2009; Haeussler *et al.*, 2012; Fig. 1).

Following the 2002 event, the U.S. Geological Survey led a multiyear effort to develop new paleoseismic sites, resulting in the development of 17 new paleoseismic sites (Fig. 1). Syntheses from these investigations along the Denali fault system report one to five paleoearthquakes at 17 different sites, 14 of which only document evidence for three or fewer earthquakes (Schwartz *et al.*, 2005, 2012; Plafker *et al.*, 2006; Seitz *et al.*, 2008; Koehler *et al.*, 2011; Personius *et al.*, 2015). Although the complete record from most of these sites is not yet published, limited earthquake chronologies are available from several sites. In particular, for the Denali fault west of the 2002 surface rupture, Schwartz *et al.* (2005) report evidence for 2–3 events ~40 km west of the Dead Mouse site in Denali National Park and Preserve. Personius *et al.* (2015) document three events and infer a fourth, most recent event, on the basis of fresh geomorphic expression of the fault scarp at the Schist Creek site, ~19 km east of the Dead Mouse site. Plafker *et al.* (2006) report three earthquakes prior to 2002 at a site in the Delta River valley, one being the 1912 M_w 7.2 earthquake first placed on the Denali fault by Carver *et al.* (2004), and the others constrained between 310–460 and 650–780 cal B.P.

We identified a narrow zone of fault-scarp morphology expressed as localized pull-apart grabens and left-stepping *en echelon* shears on a set of abandoned fluvial terraces near the eastern margin of the broad floodplain of the Nenana and Jack Rivers (Figs. 2b and 3). Initial site reconnaissance encountered abundant permafrost within the terrace surfaces except for a narrow zone above the crest of the lowest terrace riser. Our frost probe and soil auger examinations within this zone revealed 1–3 m of bedded fine-grained silt, sand, and organic-rich horizons. Three fault-perpendicular trenches were excavated across portions of the fault scarp within the permafrost-free zone on the lowest terrace (Fig. 3). This study presents the results of these investigations, including a descriptive characterization of the Denali fault at the confluence of the Nenana and Jack Rivers, classification of stratigraphic units exposed within the trenches, a synthesis of earthquake evidence at the site, and chronological modeling of paleoearthquake timing based on calibrated radiocarbon ages and sequence modeling.

We document six prehistoric earthquakes from primary evidence directly correlating with surface rupture, and one additional event on the basis of secondary structural evidence, spanning the past ~7000 yrs. As the first long paleoearthquake record west of the 2002 Denali fault earthquake

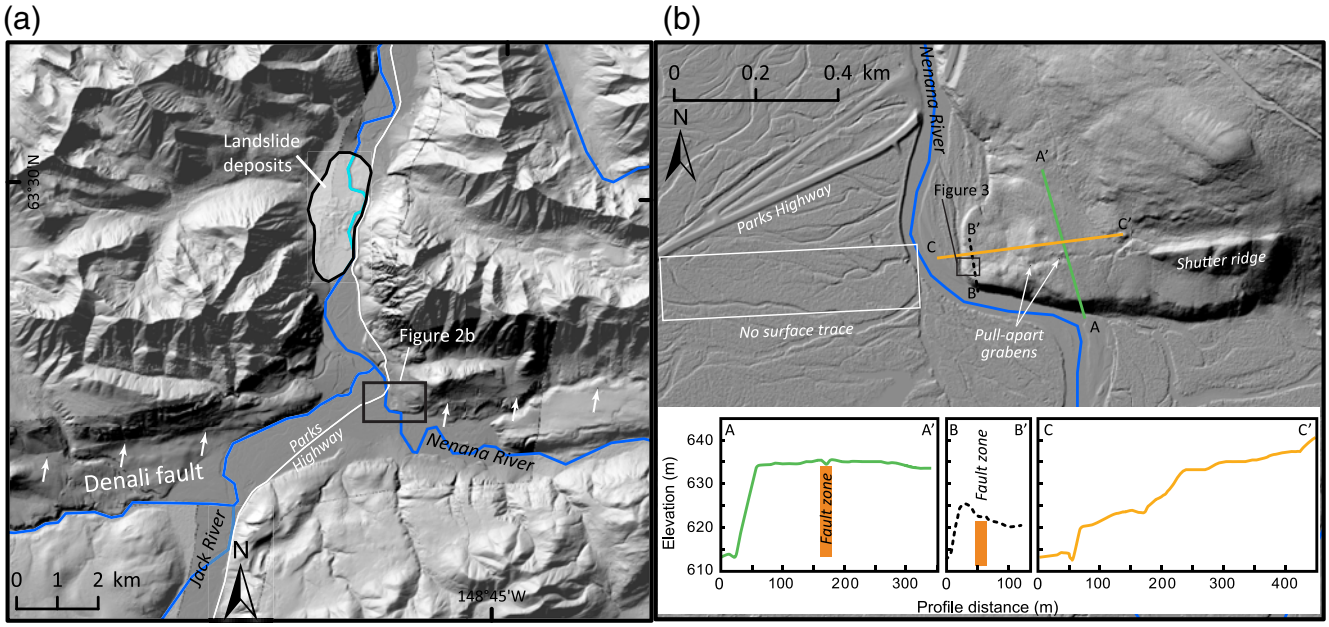

Figure 2. Location and local geomorphology of the Dead Mouse site. (a) The Denali fault (white arrows) crosses the Nenana River where the river abruptly turns to flow north across the axis of the Alaska Range. The translucent polygon illustrates the mapped extent of potentially earthquake-induced landslide deposits (Keskinen and Beget, 2005). (b) The Dead Mouse site occupies a terrace on the east bank of the Nenana River. Note the difference in fault-related geomorphic features on the east side of the river relative to young floodplain topography west of the river. Topographic profiles A–A′, B–B′, and C–C′ show the elevations of the surfaces relative to the Nenana River. In particular, A–A′ illustrates the lack of Holocene vertical offset across the Denali fault at this location. Elevation sources: (a) light detection and ranging (lidar; darker gray) from Hubbard *et al.* (2011) and Interferometric Synthetic Aperture Radar (lighter gray) from the USGS (see Data and Resources); (b) 1-m cell size lidar from Hubbard *et al.* (2011). All shaded-relief base images illuminated with azimuth/inclination of 315/45. The color version of this figure is available only in the electronic edition.

sequence, this study establishes a key dataset for infrastructural development, documenting the earthquake behavior of the Denali fault, and laying the foundation for developing the Denali fault as another test case for studies of earthquake recurrence models and potential associations between fault zone (or system) structure and rupture propagation. The Parks Highway corridor is the only railway crossing and one of three highway crossings of the Alaska Range, providing vital access to interior Alaska and Denali National Park and Preserve. Multiple proposals for natural gas pipelines targeted the Parks Highway corridor and likely would have to cross the Denali fault within 1–2 km of the Dead Mouse site. Furthermore, establishing a series of multievent paleoearthquake chronologies along the Denali fault system would create another dataset for testing and refining models of earthquake recurrence on continental strike-slip faults. In particular, with a slip rate that is ~1/2–1/3 that of the San Andreas fault we expect longer recurrence periods between earthquakes, potentially reducing the ratio of earthquake age uncertainty to interseismic interval and correspondingly decreasing the number of possible along-fault earthquake correlations.

Local Geology and Geomorphology

Quaternary glacial advances intermittently covered most of southern Alaska and the Alaska Range, with interior Alaska remaining largely unglaciated (e.g., Hamilton, 1994; Briner and Kaufman, 2008). Ice repeatedly accumulated along the axis of the Alaska Range throughout the Pleistocene, flowing to the north as lobes through the Alaska Range foothills and coalescing to the south as large ice streams. Modern glaciers emanate from the higher elevation regions of the Alaska Range. The Nenana River has its source in the Nenana Glacier on the south side of the Alaska Range, traverses the south flank of the range for ~50 km, turns north, and flows through a saddle in the axis of the Alaska Range. This river appears to have entrenched itself in the current course following deglaciation of this region at ~16 ka (Dortch *et al.*, 2010), although northward sediment transport across this portion of the Alaska Range has occurred for several million years (Thoms, 2000; Ridgway *et al.*, 2007).

Keskinen and Beget (2005) recognized a large landslide deposit ~4 km north of the Dead Mouse site (Fig. 2) and suggest it may have been triggered by an earthquake on the Denali fault 300–500 yrs ago based on lichenometric dating. Our examination of airborne light detection and ranging (lidar) and field surveys of the Denali fault across the Nenana River floodplain found no evidence of recent surface ruptures; however, a young fault scarp is clearly present along the Denali fault trace both east and west of the Nenana River (Fig. 2). Based on preserved landslide elevations, a landslide-dammed lake following the most recent earthquake on the Denali fault would have flooded the fault trace, potentially obscuring evidence for recent ruptures.

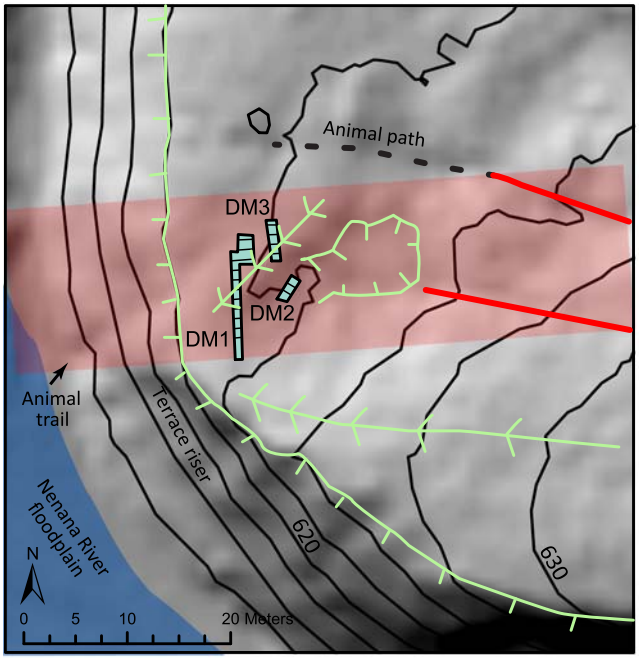

Figure 3. Detailed topographic and geomorphic map of the Dead Mouse site. The translucent east–west-oriented overlay illustrates the general width of the fault zone as based on surface morphology. Hashed boxes show the locations and names of Dead Mouse paleoseismic trenches. Two west-northwest–east-southeast-oriented lines highlight topographic troughs interpreted as relict surface fissures, although observations of active animal paths at the site show these paths both produce a similar, albeit subdued, surface morphology and occasionally occupy the coseismic topographic troughs. Hachured lines highlight prominent geomorphic features, with hachures pointing downslope. Base imagery is shaded-relief topography derived from a 0.5-m-cell-size airborne lidar digital elevation model, illuminated at with azimuth/inclination of 315/45 and with vegetation removed (Hubbard *et al.*, 2011). 2 m contour intervals. The color version of this figure is available only in the electronic edition.

Site Geomorphology

Much of the Nenana River valley near the Denali fault is characterized by glacially scoured landforms and steep bedrock slopes with alluvial fans that emanate onto the broad late Holocene floodplain. However, where the Denali fault intersects the Nenana River, there are two narrow, postglacial fluvial terraces preserved along the east side of the Nenana River (Fig. 2). Although degraded by erosion and vegetative growth, the fault trace across these terraces exhibits similar morphological characteristics as the 2002 Denali fault surface rupture (e.g., Haeussler *et al.*, 2004), including left-stepping (west-northwest trending) *en echelon*, decimeter-scale linear surface depressions, pressure ridges, and pull-apart grabens. These small-scale scarp features are superimposed on the larger, long-term geomorphic scarp (Figs. 2 and 3). Scarp preservation along the Denali fault is strongly dependent on subsurface moisture content, presence/nature of the local permafrost, and surface slope. The subtle scarp features are preserved in moderately to well-drained, seasonally frozen sediments across the geomorphically stable, subhorizontal terraces, whereas east of these terraces, only large scarp-related features are preserved across steeper slopes due to faster soil-creep processes (Fig. 2).

Two fault-perpendicular elevation profiles extracted from 0.5 m resolution airborne lidar data illustrate that there is no appreciable long-term vertical offset across the fault at this site (Fig. 2). The lack of vertical offset exhibited by profile A–A′ across the older terrace demonstrates that the apparent vertical displacement along B–B′ results from the juxtaposition of an older, higher surface against the lower, younger terrace (Fig. 2). The surficial evidence of Holocene fault displacement is constrained to a narrow zone of trough-like landforms (fissures and small pull aparts) providing the opportunity to minimize workload of trenching efforts to span the full width of fault deformation.

Methods

Initial Reconnaissance

Initial reconnaissance at the Dead Mouse site focused on attempting to find potential lacustrine deposits within the Nenana River floodplain as the product of a hypothesized landslide-dammed lake. During these investigations, we discovered a relatively thick (1–3 m) package of fine-grained sediments overlying gravelly terrace tread deposits spanning the Denali fault scarp immediately east of the Nenana River. Exploratory soil probe and auger transects demonstrated vertical offsets of the terrace tread, and initial excavations exhibited centimeter to decimeter scale bedding and abundant organic material. Additional near-surface exploration to the east along the faulted terrace surfaces encountered pervasive permafrost and active hillslope processes affecting the fault trace (Fig. 2). Minimal degradation of these geomorphic scarp features provided additional compelling evidence that structural evidence for recent earthquakes would be preserved in the subsurface. This reconnaissance established that the portion of the fault trace suitable for trenching is limited to <20 m along strike between the crest of the modern terrace riser and the onset of ice-rich permafrost to the east (Fig. 3). Therefore, our excavations targeted the fissure-like features and where soil-auger transects identified offsets of the terrace gravel in the subsurface (Figs. 2 and 3).

Paleoseismic Investigation

Initially, we hand-excavated two trenches at the Dead Mouse site (DM1 and DM2; Fig. 3). We subsequently returned to re-excavate and expand the depth and coverage of excavations to the north (the dogleg of DM1 and DM3; Figs. 3 and 4). DM1 extends ~12 m across the fault zone, with a slight jog to the east at the northern end to work around a large white spruce tree. We excavated DM2 ~2 m east of DM1 across a surface depression that we interpret as an *en echelon* fissure (Fig. 3). DM2 is oriented northeast to southwest and is 3.25 m long and 1 m wide. DM3 is located

Figure 4. Views of Dead Mouse trench 1 (DM1) and the extension. (a) North-looking view of DM1. With further northward progress impeded by the white spruce tree, we excavated the dogleg and extension (white dashed box) shown in (b). Grid lines visible on trench walls (especially on panel a) are spaced 1 m horizontally and 0.5 m vertically. Trench walls that appear as figures are labeled. The color version of this figure is available only in the electronic edition.

east of DM1 and north of DM2 (Fig. 3). It was excavated to continue our northward progression through the fault zone. The southern 2 m of DM3 overlap the northern 2 m of the DM1 extension and provides an additional meter of exposure to the north (Fig. 4). DM3 is 3.5 m long and 1 m wide. Each of these trenches provided cross-sectional exposures of generally fine-grained fluvial sediments and coseismic deformation. The depth of our excavations was limited by safety considerations and by the localized occurrence of cobbles and boulder dominated deposits. After excavating DM1 and DM3, we used a frost probe (a thin, pointed, 1.5-m-long hardened steel rod that is pushed into fine-grained sediments to detect the depth to frozen ground or coarser sediments) to record depth from trench floor to gravel contact. We probed down the center of DM1 and DM3 at half meter spacing (see Ⓔ Table S1, available in the electronic supplement to this article). With multiple measurements taken at each location and centimeter-scale measurement precision countered by an irregular trench floors and horizontal offset of the measurement points from the plane of the trench walls, we estimate the individual probe measurements to be accurate to within 20 cm.

Following trench excavation, we mapped and documented the trench walls with regard to lithologic and pedological differences in size, shape, sorting, and color, and recorded primary and secondary evidence for active faulting. We conducted our mapping on orthorectified photomosaics produced with Agisoft Photoscan Pro, following a similar process to that described in Bemis *et al.* (2014) and Reitman *et al.* (2015). We printed orthomosaics for each of the trench walls at a 1:5 scale and used these printouts as a base map to record centimeter-scale details in the field. For geospatial control, we used handheld Trimble differential Global Positioning System (decimeter-scale accuracy) for geographic positioning, and a Trimble robotic total station (centimeter-scale precision) for survey of trench boundaries, grid intersections, frost probe transects, and related target features.

Dating

The stratigraphy at the Dead Mouse site contains multiple distinct organic horizons, as well as local disseminated organic fragments. The clear stratigraphic differences and abundance of organic matter provide the framework for our chronological modeling. We collected samples of wood fragments, leaves, seeds, *in situ* charcoal, and detrital charcoal from distinct stratigraphic horizons. Our sample selection included samples that closely bracket paleoearthquake horizons as well as intervening samples to enable better characterization of the full stratigraphic sequence. Each of the samples were packaged in glass vials or wrapped in tinfoil in the field. Upon returning to the University of Kentucky radiocarbon lab, we dried samples in a low air temperature oven, and those selected for radiocarbon analysis were examined under a binocular microscope for additional documentation of sample type and quality. To prevent contamination, samples were handled with tools cleaned with methanol. Prior to lab submission, we removed modern root hairs and other macroscopic contaminants from samples by hand. We handpicked specific organic fractions (e.g., detrital charcoal, seeds, twigs, etc.) from samples that consisted of fine-grained disseminated organic material to reduce potential uncertainty from amalgamating sample material with different ages. We prepared 49 samples from a distribution spanning three trenches and 23 different stratigraphic units. After samples were cleaned we sent them to Lawrence Livermore National Laboratory's Center for Accelerator Mass Spectrometry (CAMS) and Direct-AMS for chemical pretreatment and AMS analysis.

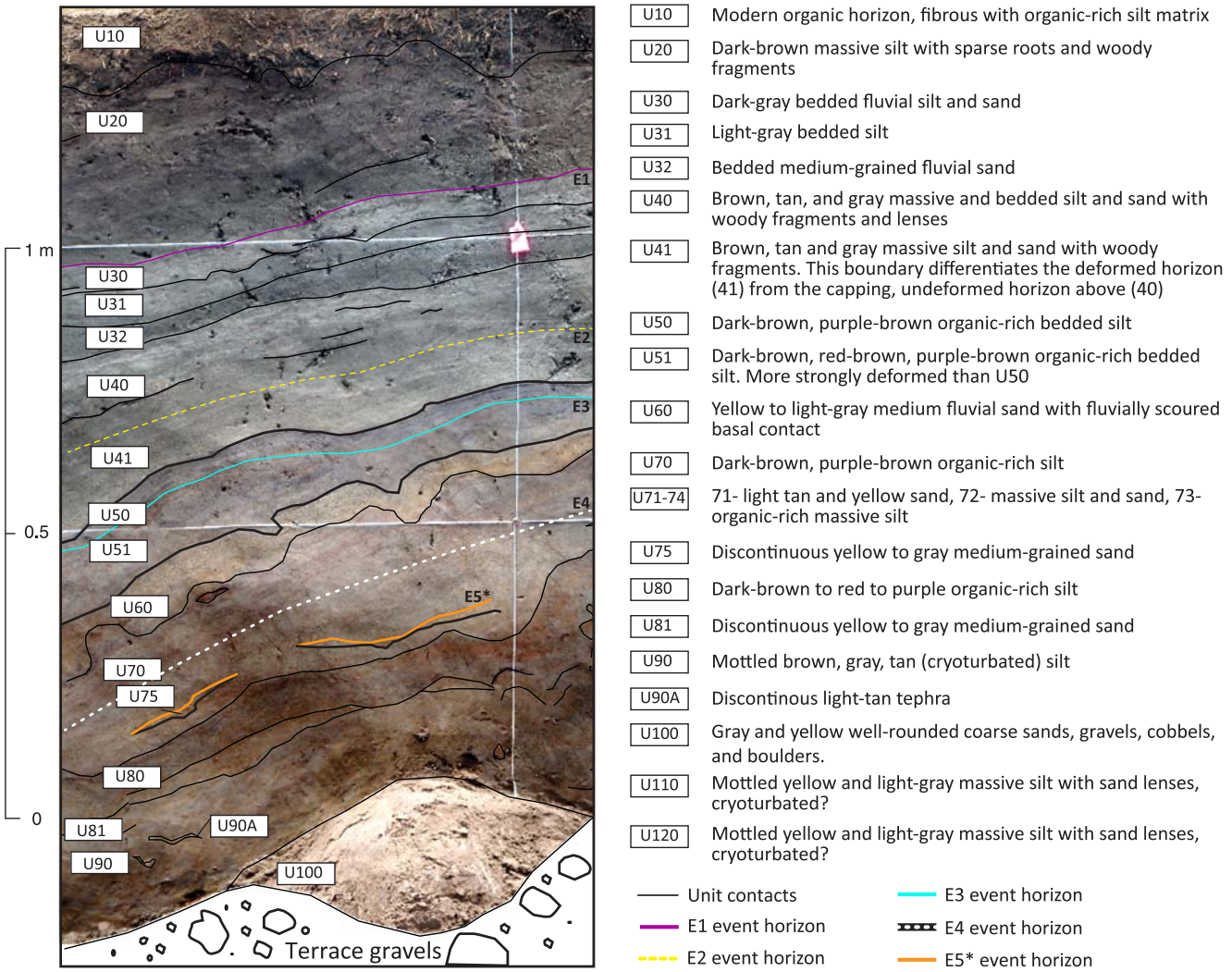

Figure 5. Generalized stratigraphic column at the Dead Mouse site providing unit names, subdivisions, and basic unit descriptions. Units U110 and U120 are not shown in this section but defined in adjacent exposures. The color version of this figure is available only in the electronic edition.

Results

Stratigraphy

Sediments at the Dead Mouse site consist of ~2–2.5 m of layered sand, silt, and organic-rich horizons deposited over fluvial sands, gravels, cobbles, and boulders (Fig. 5). Each of the three trench exposures reveal tabular and lenticular packages that are laterally continuous, yet exhibit variability in grain size, thickness, color, sorting, and organic content. Broadly, the fluvial units thicken and dip westward toward the terrace riser with the active floodplain. However, horizon thicknesses also closely correlate with vertical patterns of slip in each earthquake. The greatest vertical unit thicknesses occur directly above filled fissures and other zones of localized depression from tectonic deformation. The lower meter consists of three fining upward sequences. These three sequences are relatively similar and consist of a basal yellow–gray medium-grained well-sorted sand, fine upward and are capped by a dark-brown to purple organic-rich silt horizon. The basal sands vary greatly with lateral continuity (Fig. 5). The uppermost meter of stratigraphy is composed of a fiber-dominated modern organic-rich horizon, multiple massive silt horizons, bedded silt, and bedded sand horizons (Fig. 5). Some sections have clear continuity whereas others have a wavy discontinuous fabric. Nearly all of the basal sands have scour and fill structures, likely representing erosional gaps in sedimentation at the U60/U70, U70/U75, and U81/U90 contacts (Fig. 5). Lower in the section, a light-tan tephra is present in each of the trenches.

We classify and subdivide most sedimentary packages into lithologic units based on color, grain size, texture, sorting, and bedding (Fig. 5). Additionally, we identify multiple organic-rich horizons (Fig. 5). Our classification consists of primary and secondary units. Primary units are assigned a unit identity based on multiples of 10. Increasing unit

number corresponds with an increase in relative age and depth from the surface. Subunits are differentiated by numbers between multiples of 10 (i.e., 31, 32, 33, …). These subunits also increase numerically with relative age. In general, subunits identify lateral sedimentological change (i.e., areas of additional sedimentation) or inconsistencies with the framework of unit packages that were established on different trench walls. The site stratigraphy is divided into 23 units and subunits. We identified six event horizons where overlying undeformed units are in contact with underlying deformed units, specifically U30, U41, U51, within U70, U75, and U110 (Fig. 5). Additionally, event indicators inferred from a soil probe and the unit exposures on DM3 suggest an event horizon is located between U75 and U100 immediately below the floor of DM1 (Fig. 6a and 6b). Although U40 and U41 are lithologically indistinguishable, the contact is based on the juxtaposition of overlying horizontally undisturbed sedimentation in contact with lower deformed and disrupted textures of seismogenic origin. Also, subunit U51 represents a recognizable expansion of U50 where multiple thin organic horizons are individually distinguishable (Fig. 6a and 6b). Units U50 and U51 have lateral variability in unit thickness. These units appear to represent multiple pulses of organic development contemporaneous with variable lateral deposition of silt. The contact between these two units represents organic development that predates and postdates a prehistoric earthquake.

Subunits U71–U74 are only recognizable on the west wall of DM1. The subunits are part of a synclinal fold that was subsequently crosscut by an angular unconformity (Fig. 6b). On the southern limb of the fold, this angular unconformity crosscuts U71, U72, U73, U74, U75, and U80 (Fig. 6b). To the north, U71–U74 are crosscut but the unconformable contact continues to the north between U70 and U75. This contact represents a significant temporal gap in sedimentation.

Event Evidence

Our paleoseismic trenching at the Dead Mouse site documents multiple lines of primary evidence for six surface-rupturing events and structural evidence for one additional event. We summarize evidence below and in Table 1 for each of the seven events based on evidence type, location, and relative timing. The evidence used to define these earthquakes includes filled fissures, vertical offsets, upward fault terminations and truncations, horizontal shortening, lateral thickness changes, an angular unconformity, and distributed zones of deformation.

Event 1. Evidence for event one (E1; the most recent earthquake recorded at this site) was documented at two locations where deformation occurred above U40 (Table 1). Between 3 and 4 m on both walls of DM2, faults offset and crosscutting older deformation at depth then penetrate up through U30 as a discrete fault or a narrow shear zone (F1b, F1c; Fig. 7). On the west wall of DM2, units U30–U50 are folded and attenuated across the tip of this fault. The E1 event horizon U20 overlies the folding and increases thickness across the fold. This thickening suggests postevent deposition into a trough created by the surface deformation of E1 (Fig. 7). The east wall of DM2, however, shows no deformation above U40 and demonstrates deformation for this event is highly localized. Between 5 and 6 m on the east wall of DM1, U30–U32 are also folded (F1a; Fig. 6a). However, no discrete fault traces occur below these folds and folding is not present on the west wall of the same trench (Fig. 6b). The folding in DM1 is in contact with large dead tree roots (Fig. 6a), and it appears that units U30–32 were folded in the shallow subsurface as the tree collapsed in response to an earthquake. The subtleness of deformation and lack of broadly distributed evidence suggests this may represent an event with small surface displacement at the site.

Event 2. Evidence for event two (E2) is more distinct than E1, and it is present in each of the three trenches. In DM1, units 41 and 50 are cut by an oblique-slip fault that produces a thrust displacement, duplicating these units (F2a, F2b; Fig. 6a and 6b). The thrust fault tip is located at 6 m on the east wall and 5.5 m on the west wall of DM1 (Fig. 6a and 6b). This fault has a strike of 050°, which is ~037° oblique to the Denali fault strike, consistent with the production of a localized zone of contraction (Fig. 6a and 6b). Slight surface uplift is evident in the lidar directly above 5–6 m of DM1 and correlates to the subsurface location of thrust faulting (Figs. 3 and 6a) and the corresponding thinning of U40 across the topographic high. Evidence for E2 also occurs on the east wall of the DM1 extension (F2c, F2d; Fig. 8) and the E2 fault zone was mapped across the trench floor. The fault zone on the trench floor had a similar expression to the east wall with a texture displaying distributed deformation and bounded by planar faults. Moreover, a small fissure (F2g) located at 0 m on the east wall of DM3 breaks up to U50 and is filled with U40 (Fig. 9).

Event 3. Units U31, U32, U33, U40, and U50 dip toward two filled fissures located between 0–2 m of DM1 (Fig. 6a and 6b). These fissures are the primary evidence for event 3 (E3: F3a, F3b and F3d, F3e). They are bounded by linear fault traces, and based on their position on opposite trench walls, are oriented nearly parallel to the main trend of the Denali fault. Both of these fissures at the four cross-sectional exposures are bounded by faults, filled with sediments and are capped by U50. Units U50 and U51 vary laterally in thickness due to deposition, and multiple locations exhibit zones of expanded sedimentation (e.g., Fig. 6b). Otherwise, the majority of these two units merge into one organic-rich homogeneous unit. Although U50 and U51 merge, E3 clearly faults the lower half of these amalgamated units and is subsequently capped by a thin organic-rich horizon (U50; Fig. 6a and 6b). Therefore, we interpret the event horizon to be the top of U51 and the capping unit to be U50. Additional corroborating evidence for E3 includes an

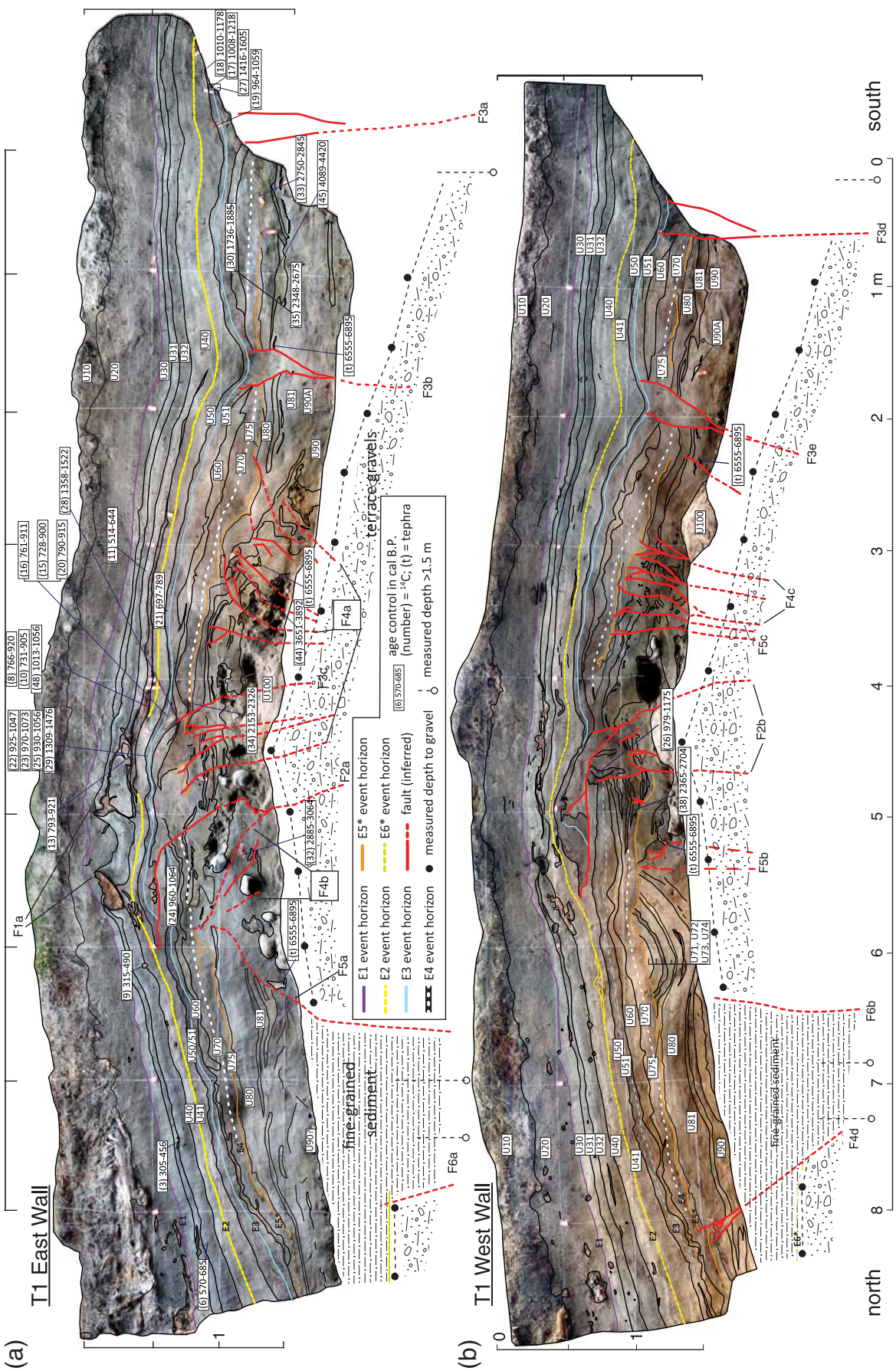

Figure 6. Photomosaics and interpretation of trench one at the Dead Mouse site (DM1). (a) East wall; (b) west wall; photomosaic rotated around a vertical axis so all trench walls have the same orientation with north on the left. Fault zones are labeled with a sequential code to identify faults associated with individual earthquakes, i.e., F4a: F, fault; 4, earthquake 4; a, first fault zone labeled for this earthquake. See Ⓔ Figures S1 and S2, available in the electronic supplement to this article, for an unannotated version of this photomosaic. The color version of this figure is available only in the electronic edition.

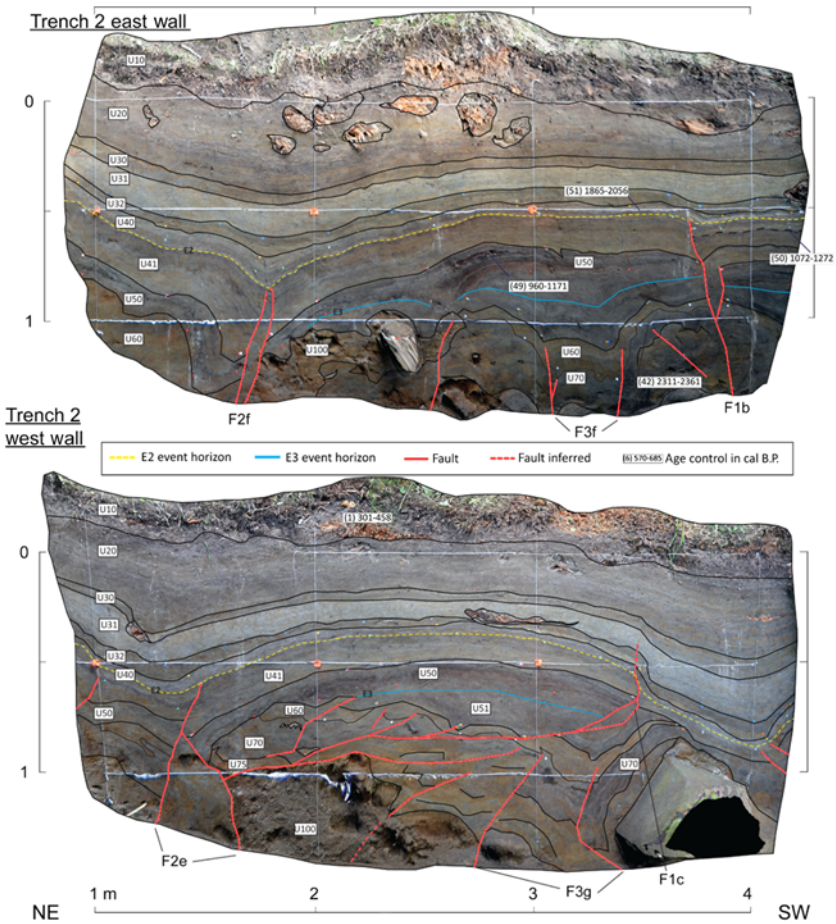

Figure 7. East and west walls of trench two at the Dead Mouse site (DM2EW and DM2WW). West wall photomosaic rotated around a vertical axis so all trench walls have the same orientation with north on the left. Fault zones are labeled with a sequential code to identify faults associated with individual earthquakes (i.e., F4a: F, fault; 4, earthquake 4; a, first fault zone labeled for this earthquake). See Ⓔ Figure S3 for an unannotated version of this photomosaic. The color version of this figure is available only in the electronic edition.

upward fault termination at the U50/51 boundary on the east wall of the DM1 extension near 10 m (F3h; Fig. 8). This location shows a clear juxtaposition of units bounded by a curved fault trace and a thin tephra with ~0.5 m of vertical offset (F3h; Fig. 8).

Event 4. The primary evidence for event 4 (E4) occurs as numerous small offsets and associated folding of the basal contact of U70 (Table 1). These faults are best expressed by faults F4a–F4d in both walls of DM1 (Fig. 6a and 6b) and fault F4e on the east wall of DM3 (Fig. 9). Although there is not a persistent stratigraphic boundary within this unit that clearly corresponds with these fault terminations, the uppermost few centimeters of U70 are not faulted or deformed, providing a means for separating pre- and postevent radiocarbon samples from within U70.

Event 5. The most distinctive evidence for event 5 (E5) is an angular unconformity below U70 on the east wall of DM1 between 5 and 7 m (Fig. 6b). Synclinal folding of the units below the unconformity preserves several units (U71–74) that are absent from elsewhere in the trench. Several faults appear to be associated with this event due to proximity to E5-related folding and truncation by the unconformity. Faults F5a and F5b appear to record the greatest displacement due to the juxtapositioning of different units and distributed deformation, whereas the other F5 faults exhibit apparently minor offsets.

Event 6. Our interpretation of this event is based on a >1 m vertical offset in the fluvial gravels between 6 and 8 m of DM1 (F6a, F6b; Fig. 6a and 6b). We used a frost probe to record the top of the gravel contact and were able to identify the offset by inserting the full length of the probe (1.5 m) without contacting the fluvial gravel. This vertical offset is not represented in the overlying exposed stratigraphy. Structurally, the overlying sediments are subhorizontal and folded fine-grained beds that appear to generally dip to the north but are highly disrupted due to tectonic deformation or cryoturbation. Stratigraphically, this event can be constrained to below U81 and above the top of the U100 fluvial gravel contact.

Event 7. Event 7 (E7) is the oldest event and evidence is only expressed at one location on the east wall of DM3 (F7a; Fig. 9). The event evidence includes upward fault terminations, and vertical offsets are not reflected in overlying deposits (F7a; Fig. 9). The faults and structural evidence are distributed over 75 cm and are capped by reworked rounded sand to boulder-sized matrix-supported sediment. Multiple fault strands are capped by U100, and these are distinct from fault trace F2g, which displaced U100 during a younger earthquake (Fig. 9). As a high-energy deposit, the basal contact of U100 appears erosional.

Earthquake Chronology

The relative sequence of earthquakes at the Dead Mouse site is well defined through superposition of stratigraphic horizons and the crosscutting relationships of faults and folds. We subdivide the stratigraphy into a framework of units to provide context for the description of superposition and chronological modeling. We identify units based on sedimentological differences to correlate strata across the site. To place stratigraphic horizons and earthquakes within an absolute age framework, we incorporated radiocarbon

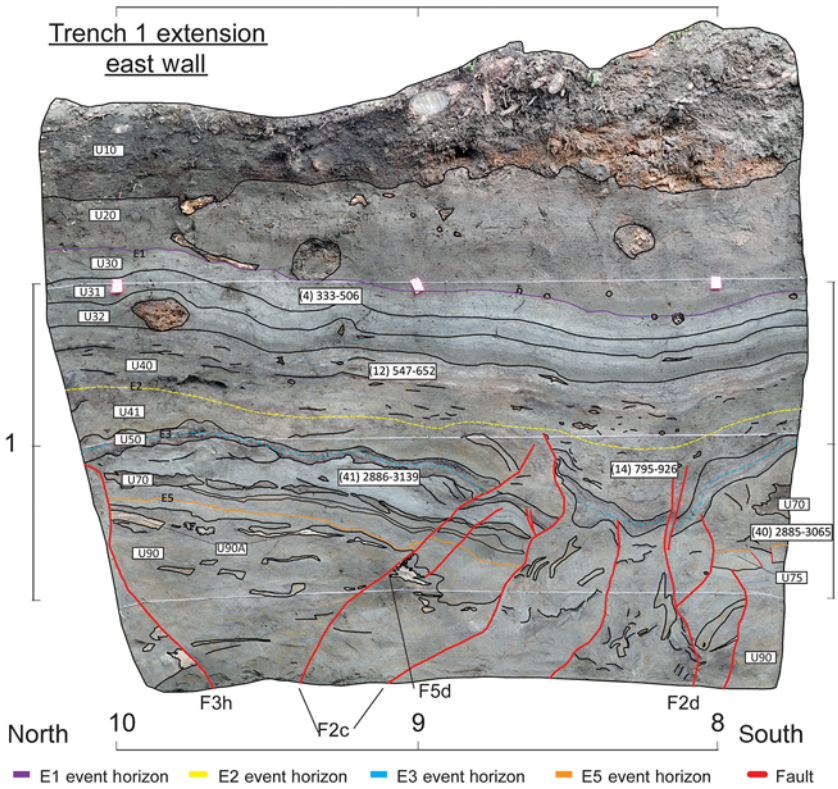

Figure 8. East wall of the northward extension of trench one at the Dead Mouse site (DM1extEW). This wall is aligned with the north end of DM1EW (Fig. 6a) but offset ~1 m to the east. Fault zones are labeled with a sequential code to identify faults associated with individual earthquakes (i.e., F4a: F, fault; 4, earthquake 4; a, first fault zone labeled for this earthquake). See Ⓔ Figure S4 for an unannotated version of this photomosaic. The color version of this figure is available only in the electronic edition.

samples collected through the stratigraphic section and a tentatively correlated tephra into a stratigraphic age model (model code provided in the Ⓔ electronic supplement). Using the Bayesian stratigraphic modeling approach, we calculated probability density functions for radiocarbon samples and event ages within the stratigraphy at the Dead Mouse site with OxCal 4.2.4 and the calibration model of Bronk Ramsey (2008, 2009), Lienkaemper and Ramsey (2009), and Reimer *et al.* (2013) (see Ⓔ Fig. S7). Miscorrelation of units between trenches would be the largest source of error in this relative sequence. However, the close proximity of the trenches and the sedimentologically distinct nature of the faulted horizons and sequences produce units that are well correlated and internally consistent above U70 and exhibit greater variability below U70 (see Ⓔ Fig. S7).

Radiocarbon Constraints. Organic-rich horizons are abundant at the Dead Mouse site and offer ample opportunity for stratigraphic age control, especially in the upper meter of stratigraphy. Sampled materials consisted of woody macrofossils, detrital charcoal, and *in situ* charcoal with individual cleaned and submitted sample masses varying between 9 and 339 mg. The majority of charcoal samples did not show evidence of significant degradation prior to deposition (e.g., rounding and weathering). Therefore, we infer that the samples were either derived from local fire events or that their inherited age due to transport was minimal. Our age chronology at the Dead Mouse site is constrained by 49 AMS radiocarbon analyses collected from a broad stratigraphic distribution in each of the three trenches (Table 2).

Radiocarbon analyses are consistent with previously discussed relative age constraints and the defined sequence of stratigraphic units. Forty-six of 49 sample age results fit within the stratigraphic framework of this site. Only three sample ages contradicted the principle of superposition and thus were excluded from the sequence model (Table 2). For the purpose of our sequence modeling, we grouped stratigraphic units U30, U31, U32, and U41 because there are no events within this interval and the units cover a relatively short period of time. Within this group of units are several samples from dead roots that produce younger ages than the containing unit, but that are consistent with the overlying units. Given that the trees in this environment are characteristically shallow rooted and major roots like those sampled here are unlikely to penetrate more than a few centimeters into the units below the organic surface layer at the time of growth (e.g., Strong and Roi, 1983), these ages produce a locally inverted, but predictable, age relationship (Table 2).

Tephra. The presence of a volcanic tephra within the lowest half meter is persistent in DM1 and recognizable in DM3. We have not analyzed the geochemistry, but the geographic location and stratigraphic position below U80 makes it potentially correlative with either the Hayes set H tephra (3910–4205 cal B.P.) or the Oshetna tephra (6555–6895 cal B.P.), which have been identified in the region (Wallace *et al.*, 2014; Davies *et al.*, 2016). The tephra within the trench stratigraphy is laterally discontinuous and occurs in ~1–2-cm-thick lenses and stringers that are deformed into ~1–10-cm-long wavy horizons. Additionally, in several locations the tephra appears to be horizontally shortened and vertically thickened. Although the tephra tends to be laterally discontinuous, the stratigraphic position remains consistent throughout DM1, providing a unique marker horizon within the deeper stratigraphy where chronological constraints are limited.

Dead Mouse Earthquake Chronology. The calibrated radiocarbon ages (cal B.P.) of our samples demonstrate a gradual increase in age from U10 to U60, whereas multiple

Table 1

Event Evidence for Dead Mouse Site Paleoearthquakes

Event	Trench Wall	Event Evidence	Event Horizon	Capping Horizon	Trench Location (m)	Fault Label	Description and Interpretation of Event Evidence
E1	DM1EW	fold	U30	U20	4–6	F1a	Folded well-bedded fine to coarse sand. Correlates with localized surface uplift
E1	DM2EW	utf	U31l	U31u	4	F1b	Upward decrease in displacement across fault trace
E1	DM2WW	utf	U30	U20	3.5	F1c	Fault diffuses into distributed shear within units 31 and 30
E2	DM1EW	vo, short	U41	U40	6	F2a	Thrust fault duplicates U50 and U41
E2	DM1WW	vo, short	U41	U40	5.5	F2b	Fault plane appears to be a right-stepping oblique fault with localized contraction
E2	DM1EWext	utf, fis, vo	U41	U40	9–9.5	F2c, F2d	Broad fault zone deformation
E2	DM2EW	utf, fold	U41	U40	2	F2f	Offset and folding of units 41 and below. U 40 fills depression postfaulting
E2	DM2WW	utf, vo	U41	U40	1.5	F2e	Vertical offset and thickness changes across fault
E2	DM3EW	utf, fis	U41	U40	0.2, 2.8	F2g, F2h	Faults offset base of U41
E3	DM1EW	utf, fis	U51	U50	0–1.8	F3a, F3b	Filled fissures
E3	DM1EW	utf, vo	U60	U50	4	F3c	U51 thickens across top of fault that displaces U60
E3	DM1WW	utf, fis	U51	U50	0.5– 2	F3d, F3e	Filled fissures
E3	DM2EW	utf, fold	U51	U50	3–3.5	F3f	Faults terminate toward base of U51, U51 significantly folded over these faults
E3	DM2WW	utf, fis	U51	U50	2.5–3.5	F3g	Faults terminate toward base of U51, U51 significantly folded over these faults
E3	DM1EWext	utf, vo	U51	U50	10	F3h	Poorly exposed fault termination. Tephra vertical offset ~0.5 m
E4	DM1EW	utf	U70l	U70u	3–4.5	F4a	Numerous small-offset faults that displace U75 and lower U70
E4	DM1EW	utf, dis, short	U70l	U70u	5–6	F4b	Faults and distributed deformation that deforms U75 and lower U70 appears locally thickened and eroded
E4	DM1WW	utf	U70l	U70u	3–3.5	F4c	Numerous small-offset faults that displace U75 and lower U70
E4	DM1WW	utf	U70l	U70u	8	F4d	Fault offsets U75 and lower U70
E4	DM3EW	utf	U70l	U70u	0.5–1	F4e	Numerous small-offset faults that displace U75 and lower U70
E5	DM1EW	utf, dis,	U80	U70	2.5–3.5	F5a	Units below U70 juxtaposed against distributed deformation
E5	DMIWW	dis, fold, ang	U71	U70l	5–6	F5b	Distributed deformation near fault, folded units 71–74, angular unconformity
E5	DM1WW	utf	U75	U70	3.5	F5c	Small displacement faults overlain by U70l
E5	DM1EWext	utf, vt, short	U75	U70	9	F5d	Prominent shortened and thickened tephra corresponds with significant thickness change of U75 not consistent with apparent offsets of overlying units
E6	DM1EW	vo, vt	U100	U81	6.5–7.5	F6a	Subsurface evidence for vertical offset U100 with no vertical offset in overlying fine-grained sediments
E6	DM1WW	vo	U100	U81	6.5	F6b	Subsurface evidence for vertical offset U100 with no vertical offset in overlying fine-grained sediments
E7	DM3EW	utf, vo	U110	U100	2–2.7	F7a	Several faults terminate against base of U100

Wext, west extension; vo, vertical offset; utf, upward terminating fault; fis, fissure; dis, distributed deformation; short, horizontal shortening; fold, fold; vt, vertical thickening; ang, angular unconformity; l, lower section of unit; u, upper section of unit.

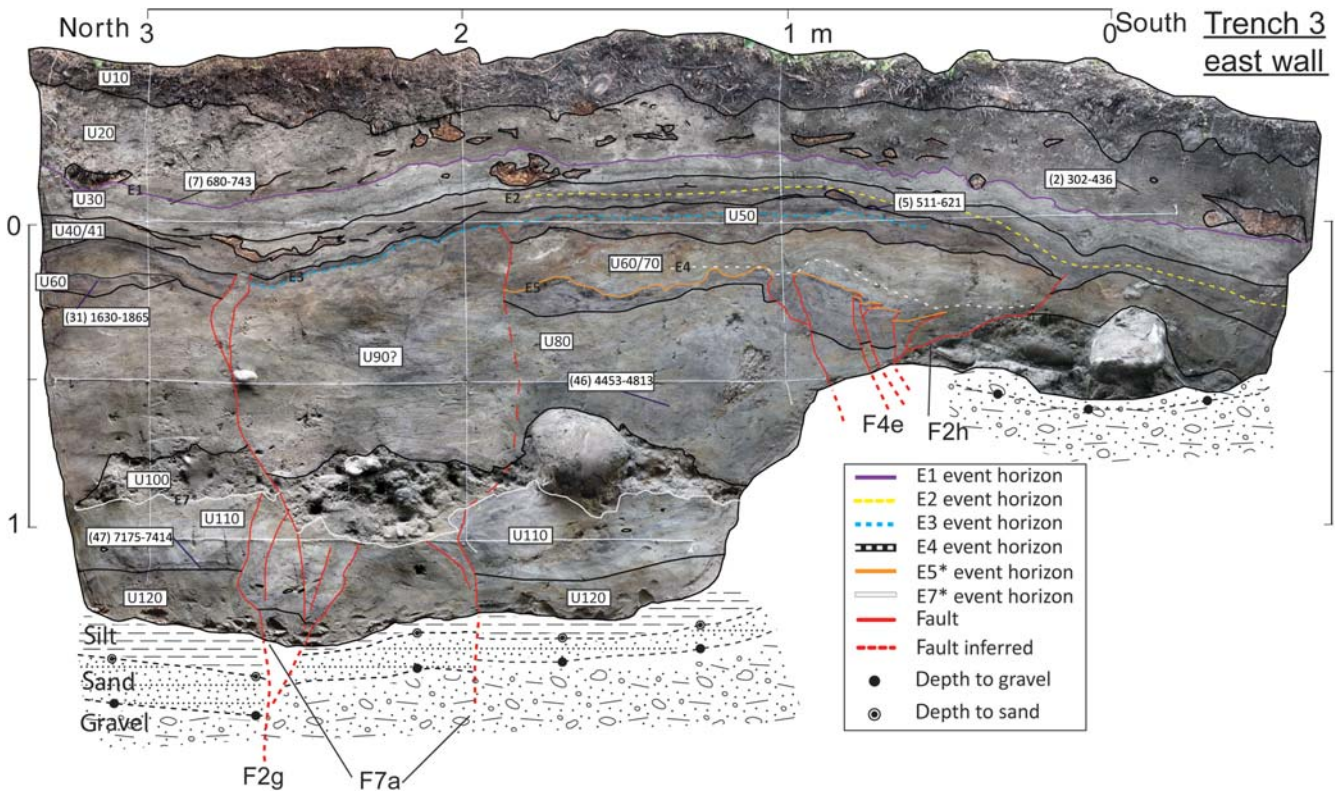

Figure 9. East wall of trench three at the Dead Mouse site (DM3EW). The west wall of this trench did not provide any event evidence and is thus provided as Ⓔ electronic supplement. Fault zones are labeled with a sequential code to identify faults associated with individual earthquakes (i.e., F4a: F, fault; 4, earthquake 4; a, first fault zone labeled for this earthquake). See Ⓔ Figure S5 for an unannotated version of this photomosaic. The color version of this figure is available only in the electronic edition.

age gaps occur for samples from U70 to U120 (Table 2; Ⓔ Fig. S7). Our sequence model constrains mean ages for paleoearthquakes at the Dead Mouse site at 388, 807, 1282, 2652, 3402, 5673, and 6987 cal B.P. (Table 3; also Ⓔ Fig. S7).

Time intervals between our documented earthquakes vary greatly at this site. The two intervals defined by the most recent three earthquakes have similar durations, with the E1–E2 interval at 419 ± 80 yrs and the E2–E3 interval of 475 ± 130 yrs (Table 4). The modeled intervals between earthquakes E3–E7 are longer and display greater uncertainties, with intervals for E3–E4 at 1370 ± 230 yrs, E4–E5* at 750 ± 450 yrs, E5*–E6* at 2271 ± 1170 yrs, and E6*–E7* at 1314 ± 1100 yrs (Table 4). The E3–E4 interval occurs in a portion of the stratigraphic section that represents a lower sedimentation rate, where ~0.2 m of sedimentation occurred over approximately the same amount of time as uppermost 0.7–1 m of sedimentation (e.g., Figs. 7 and 8).

Discussion

Earthquake Event Interpretations

The 2002 Denali fault earthquake sequence provides the only direct example of geomorphologic fault expression from a historic surface rupture on the Denali fault. From this event, Eberhart-Phillips *et al.* (2003) and Haeussler (2009) describe offset landforms, extensional and contractional stepovers, *en echelon* fissures, and Riedel shears in snow, glacial ice, and surficial deposits/vegetation. According to their observations, dextral displacements comprised the majority of the observable offsets and vertical-slip components were localized and minimal (Eberhart-Philips *et al.*, 2003; Haeussler, 2009). Others document mean right-lateral offsets of 4.5–5.1 m and a maximum offset of 8.8 m (Haeussler *et al.*, 2004). These studies provided a spectrum of modern surface-rupture examples in varying near-surface materials that enable better interpretation of paleoearthquake evidence at the Dead Mouse site. For example, observations of sheared and toppled trees following the 2002 earthquake (e.g., Carver *et al.*, 2004; Haeussler *et al.*, 2004) illustrated how the lateral strength of roots can distribute coseismic deformation at shallow stratigraphic levels without faulting or folding occurring directly underneath. The evidence for E1 reflects this situation in which our exposures encountered only minor faulting in one location but substantial deformation associated with now dead and partially decayed tree roots in the same units. The evidence for the preceding event E2 follows patterns displayed by meter-scale contractional stepovers during the 2002 earthquake where the surficial organic mat detached from underlying sediments and was thrust over

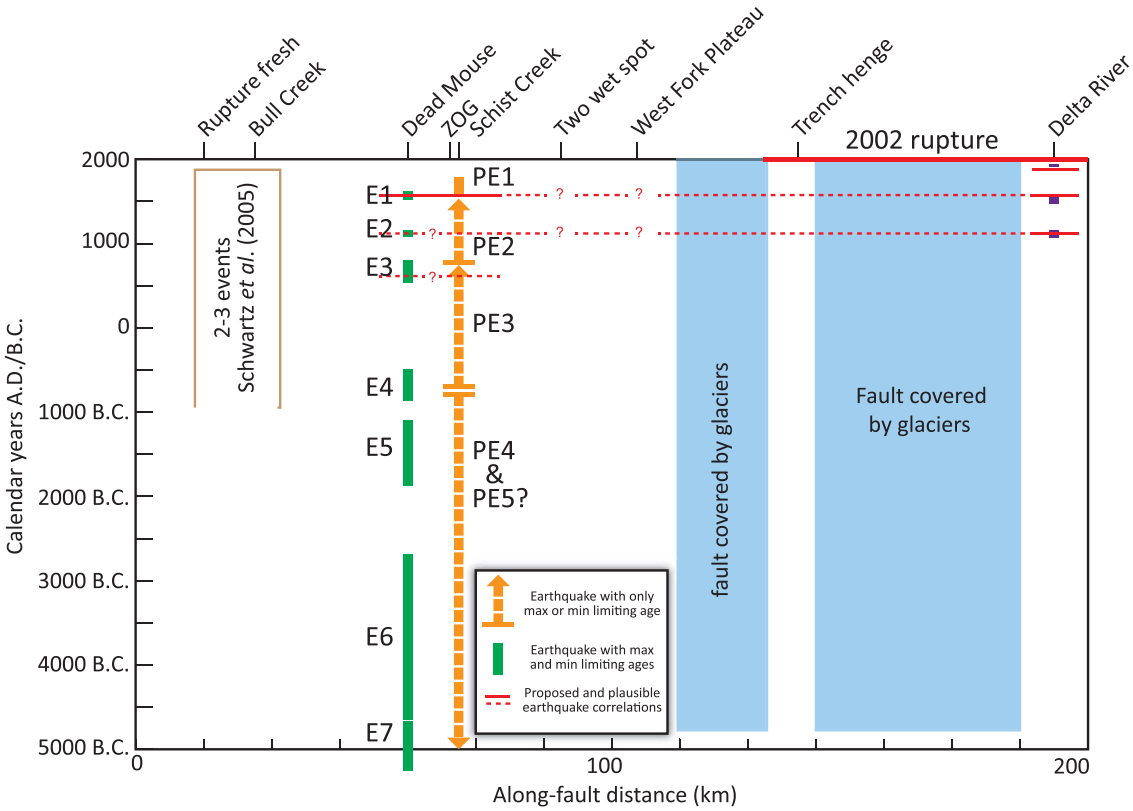

Figure 10. Space–time diagram illustrating the along-fault distribution of paleoseismic sites on the Denali fault west of the Delta River (Fig. 1) and the published paleoearthquake records. The limited data from other along-fault paleoseismic sites accommodate a couple potential event correlation scenarios between Dead Mouse (this study) and Schist Creek (Personius *et al.*, 2015), including the E1-PE1, E2-PE2, and E3-PE3 correlations as shown. Alternatively, the age control at Schist Creek permits correlations between E3-PE2 and E4-PE3. In this scenario, there is not an E2 correlative earthquake at Schist Creek, or evidence for such an event was missed at that site. The Delta River site (Plafker *et al.*, 2006) has plausible earthquake correlations with earthquakes E1 and E2 at Dead Mouse. Vertical bars show the uncertainty associated with the timing of individual earthquakes. The color version of this figure is available only in the electronic edition.

itself through oblique lateral slip. This contractional pattern contrasts with the development of multiple extensional fissures exhibited by E3 (e.g., Fig. 6a and 6b). Although the original rupture morphology of E4 and older earthquakes are more difficult to interpret, the patterns from E1, E2, and E3 demonstrate variable surface-rupture patterns that likely result from both surficial conditions at the time of the earthquake (e.g., seasonal freezing, moisture content, and location of trees) and characteristics of the earthquake itself (e.g., amount of coseismic slip).

Earthquake Record Completeness and Correlations

The radiocarbon age progression (Table 2; Ⓔ Fig. S7) suggests sedimentation at the site without appreciable erosion from ~300 to 3000 cal B.P., which is consistent with the lack of obvious unconformities in this portion of the stratigraphic section. The four most recent events occurred within the period of continuous sedimentation, which indicates that these four events likely represent the complete record of surface-rupturing events for the Denali fault at the Dead Mouse site from the present day back to 3000 cal B.P. In contrast, beyond ~3000 cal B.P. the stratigraphy is punctuated by periods of erosion or nondeposition, and therefore the timing of the three oldest events (> 3000 cal B.P.) are less well constrained because they correspond with temporal gaps in our age control, exhibit greater uncertainty in stratigraphic relationships, and likely are missing intervening earthquakes.

Comparing this record of earthquakes to the limited data available from other paleoearthquake sites along this portion of the Denali fault illustrates potential correlations of event timing at the Dead Mouse site, Schist Creek site, and the Delta River site (Fig. 10). The most recent event (E1) at the Dead Mouse site correlates with the timing of the most recent event (PE1) that Personius *et al.* (2015) infer from youthful fault geomorphology at the Schist Creek site (11 km east of Dead Mouse site) and the penultimate earthquake at the Delta River site (Plafker *et al.*, 2006). This correlation would indicate a rupture length of at least 150 km and will be testable with the unpublished records from several intervening sites (Fig. 10). The penultimate earthquake at the Schist Creek site (PE2) could correlate to either E2 or E3 at the Dead Mouse site due to the limited age constraints at the Schist Creek site (Fig. 10). If E2 correlates with PE2, it

Table 2
Radiocarbon Sample Data and Calibrated Ages from the Dead Mouse Site

Sample Name	Lab ID*	Trench	Wall	Unit	Sample Type†	^{14}C Age (yr B.P. at 1σ)‡	δ^{13}C	Age (cal B.P.)§	Trench Log Code
DFDM2WW 2A-M2	CAMS 173716	2	W	10	w	305 ± 25	−25.3	301–458	1
DM3EW0.86,A5	D-AMS 013423	3	E	20	c	305 ± 19	−24.0	302–436	2
DM1EW7.5C31	D-AMS 013292	1	E	30	w	312 ± 21	−24.4	305–456	3
DM1extEW9.09,C46	D-AMS 013420	1ext	E	30	w	393 ± 19	−27.4	333–506	4
DM3EW1.68,A3	D-AMS 013287	3	E	30-32	w	524 ± 22	−22.6	511–621	5
DM1EW8.24,C18	D-AMS 013419	1	E	31-32	w	705 ± 20	−22.6	570–685	6
DM3EW3.9,A7	D-AMS 013424	3	E	30-32	w	803 ± 20	−23.9	680–743	7
SB-DFDM1-01	D-AMS 002085	1	E	40	w	916 ± 27	−9.8	766–920	8
DM1EW6.14,B7	D-AMS 013291	1	E	32	w	349 ± 23	−19.0	315–490	9
SB-DFDM1-02	D-AMS 002086	1	E	40	w	882 ± 25	−30.7	731–905	10
PTDM1-3	D-AMS 001361	1	E	40	c	551 ± 36	−25	514–644	11
DM1extEW8.88,C18	D-AMS 013289	1ext	E	40	w	607 ± 22	−16.7	547–652	12
PTDM1-1	D-AMS 001360	1	E	41	w	937 ± 27	−20.0	793–921	13
DM1extEW 8.18,D46	CAMS 173707	1ext	E	41	w	930 ± 25	−27.2	795–926	14
DM1EW4.26,C42	D-AMS 013422	1	E	40-50	w	871 ± 21	−23.9	728–900	15
DM1EW4.55,B4D	D-AMS 013426	1	E	40-50	w	905 ± 22	−23.3	761–911	16
SB-DFDM1-5c	D-AMS 002089	1	E	50	c	1186 ± 27	−24.9	1008–1218	17
SB-DFDM1-5d	D-AMS 002091	1	E	50	c	1174 ± 21	−28.7	1010–1178	18
PTDM1-4	D-AMS 001362	1	E	50	c	1110 ± 22	−26.9	964–1059	19
DM1EW4.26,C37	D-AMS 013286	1	E	50	w	926 ± 22	−19.1	790–915	20
DM1EW3.60,B38	D-AMS 013290	1	E	50	w	842 ± 22	−20.2	697–789	21
DM1EW4.55,B4C	D-AMS 013294	1	E	50	c	1052 ± 22	−23.2	925–1047	22
DM1EW4.55B4B	D-AMS 013425	1	E	50	c	1132 ± 19	−25	970–1073	23
DM1EW 5.29,C40	CAMS 173703	1	E	50	c	1110 ± 25	−26.0	960–1064	24
DM1EW 4.55,B4A	CAMS 173708	1	E	50	c	1075 ± 30	−25.4	930–1056	25
DM1WW 4.72,C8	CAMS 173712	1	W	50	c	1155 ± 35	−25	979–1175	26
SB-DFDM1-5a	D-AMS 002090	1	E	51	w	1632 ± 25	−25	1416–1605	27
DM1EW4.24,C32	D-AMS 013285	1	E	51	w	1534 ± 23	−23.7	1358–1522	28
DM1EW4.55,B4AW	D-AMS 013293	1	E	51	w	1493 ± 27	−21.8	1309–1476	29
DM1EW 0.66,C-6	CAMS 173702	1	E	60	w	1885 ± 25	−27.3	1736–1885	30
DM3EW 4.18,B32	CAMS 173701	3	E	60	w	1825 ± 35	−26.8	1630–1865	31
SB-DFDM1-13a‖	D-AMS 002087	1	E	unkn	w	2859 ± 25	−27.2	2885–3064	32‖
SB-DFDM1-10b	D-AMS 002088	1	E	70l	c	2674 ± 25	−27.7	2750–2845	33
DM1EW4.19,C21	D-AMS 013421	1	E	70u	w	2221 ± 28	−17.6	2153–2326	34
DM1EW 0.90,C-15	CAMS 173713	1	E	70u	w	2395 ± 25	−26.8	2348–2675	35
DM1WW 4.9,C5	CAMS 173704	1	W	70u	w	2455 ± 25	−25.8	2365–2704	38
DM1WW 5.44,D46	CAMS 173705	1	W	70	w	2395 ± 25	−25.5	2348–2670	39
DM1extEW 7.8,D5	CAMS 173710	1ext	E	70l	c	2860 ± 25	−25.0	2885–3065	40
DM1extEW 9.15,D3	CAMS 173711	1ext	E	70l	c	2875 ± 30	−26.6	2886–3139	41
DFDM2EW 14A-M3	CAMS 173718	2	E	70u	c	2320 ± 25	−25.0	2311–2361	42
DM3WW1.66,B25	D-AMS 013288	3	W	70?	w	620 ± 25	−21.5	551–658	43
DFDM1EW 10A-M3-01	CAMS 173715	1	E	80	w	3515 ± 40	−25	3651–3892	44
DM1EW 1.20,C-35	CAMS 173706	1	E	80	w	3840 ± 60	−25	4089–4420	45
DM3EW 2.36,C40	CAMS 173714	3	E	80	c	4100 ± 30	−23.8	4453–4813	46
DM3EW 3.8,C-7	CAMS 173709	3	E	110	w	6345 ± 30	−28.1	7175–7414	47
PTDM1-2‖	BL 333104	1	E	40	w	1080 ± 30	−25.2	1013–1056	48‖
DFDM2EW 10A-M2	CAMS 173717	2	E	50	w	1125 ± 25	−24.8	960–1171	49
DFDM2EW 8A-M4	CAMS 173719	2	E	50	w	1245 ± 35	−25	1072–1272	50
DFDM2EW 6B-M3‖	CAMS 173720	2	E	unknown	w	1995 ± 40	−25	1865–2056	51‖

*Radiocarbon lab codes: CAMS, Lawrence Livermore National Labs Center for Accelerator Mass Spectrometry; D-AMS, DirectAMS; BL, Beta Analytic.
†w, wood; c, charcoal.
‡The quoted age is in radiocarbon years using the Libby half-life of 5568 yrs and following the conventions of Stuiver and Polach (1977). Sample preparation backgrounds have been subtracted, based on measurements of radiocarbon-dead standards pretreated in parallel with samples.
§Ages calibrated with OxCal v.4.2 (Bronk Ramsey, 2009) using the IntCal 13 calibration curve (Reimer *et al.*, 2013), with ages quoted at 2σ errors.
‖Denotes samples not included in the OxCal model.

permits another rupture scenario identical to the E1 correlation with the Delta River site, suggesting the possibility of repeated > 150-km-long ruptures. However, Personius *et al.* (2015) argue that if deposition at their site quickly followed the PE2 surface rupture, the age for PE2 would be closer to the maximum limiting age. In this scenario, PE2 would more likely correlate with E3 at Dead Mouse and would not have a known correlative earthquake at the Delta River site (Fig. 10).

Table 3
Modeled Event Timing

Event	Modeled cal B.P. From	Modeled cal B.P. To	Mean cal B.P.	Modeled cal A.D./B.C. From	Modeled cal A.D./B.C. To	Mean cal A.D./B.C.
E1	442	319	388	1509	1632	1562
E2	853	764	807	1098	1187	1143
E3	1392	1160	1282	559	791	668
E4	2805	2460	2652	**856**	**511**	**703**
E5*	3790	3010	3402	**1841**	**1061**	**1453**
E6*	6676	4632	5673	**4727**	**2683**	**3724**
E7*	7281	6668	6987	**5332**	**4719**	**5038**

Asterisks denote the paleoearthquakes that may have missing events in the preceding interseismic interval based on stratigraphic relationships. Bold numbers indicate cal B.C. ages.

Table 4
Intervals between Known Earthquakes at the Dead Mouse Site

Interevent Interval	Interval Duration (yrs) From	Interval Duration (yrs) To	Mean Duration (yrs)
E1–E2	345	501	419
E2–E3	344	596	475
E3–E4	1140	1578	1370
E4–E5*	298	1196	750
E5*–E6*	1097	3439	2271
E6*–E7*	218	2412	1314

The oldest three earthquakes recorded at the Dead Mouse site do not directly correspond with other known events along this section of the Denali fault but do overlap one or more poorly constrained events at the Schist Creek site. Although the ages are not well constrained, earthquakes E6 and E7 are the oldest earthquakes currently recognized on the entire Denali fault system and provide optimism for the ability to establish longer earthquake chronologies elsewhere along the fault.

The Dead Mouse site exhibits recurrence intervals of 419 ± 80 and 475 ± 130 yrs for the E1–E2 and E2–E3 interseismic periods, respectively (Table 4). With the most recent earthquake at our site occurring between 1510 and 1634 cal A.D. (Table 3), this portion of the Denali fault is currently within the range of the last two recurrence periods. However, the E3–E4 recurrence period is much longer (1370 ± 230 yrs), suggesting significant variability in the recurrence interval at this site. The interseismic intervals between E4–E7* do not provide compelling constraints on recurrence interval length or variability due to the potential for missed earthquakes within those intervals. The 300–600-yr recurrences exhibited by the most recent three earthquakes is consistent with other interpretations of recurrence timing from sites eastward along the Denali fault system by Plafker *et al.* (2006) and Schwartz *et al.* (2012) (Fig. 10).

Improvement upon the chronological record and event history at the Dead Mouse site may require additional dating methods as well as further expansion of trenching efforts. We collected a suite of samples from our trench stratigraphy for luminescence dating during summer 2015 and anticipate that future analysis of these samples will improve our chronological constraints, especially in the older stratigraphy associated with events E5, E6, and E7. These older events are bounded by units that suffer from oxidation of the organic material, reducing the availability of material for radiocarbon dating. Although our excavations did not extend into clearly undeformed stratigraphy outside the fault zone, based on the distribution of deformation illustrated in high-resolution bare-earth topography and our field observations we suspect that undeformed stratigraphy occurs within 1–2 m of our exposures. Furthermore, based on the distributed nature of faulting from recent earthquakes through the site, it is unlikely that a recent surface rupture would have occurred within this narrow distance without creating additional deformation that would have been captured by our excavations. Expansion of trenches to the north and additional parallel excavations across the main fault zone are the most promising targets for further work at the site because we expect much of the older stratigraphy to be obliterated by cryoturbation along the fault to the east, and the higher elevation/higher relief sites would be lacking sufficient stratigraphy.

Conclusions

We excavated three trenches at the Dead Mouse site on the Denali fault to establish a robust paleoearthquake chronology west of the 2002 Denali fault earthquake sequence surface-rupture extent. Mapping of the trench walls supplemented by soil probe measurements along the trench floors provides structural and stratigraphic evidence for seven paleoearthquakes. Forty-nine radiocarbon ages constrain the age of the stratigraphic section. The upper portion of the stratigraphy contains evidence for four earthquakes during the past ~3000 yrs. Based on the radiocarbon age progression and a lack of unconformities, we interpret this to record the complete paleoearthquake record at this site during this interval. The lower stratigraphic section contains evidence for three earthquakes between ~3000 and 7000 yr B.P.; however, due to potential overprinting of deformation by younger events, poorer exposure/stratigraphic preservation, and gaps in the stratigraphic record, we suspect there are missing earthquakes within the earthquake chronology prior to E4. The seven earthquakes at the Dead Mouse site represent the longest earthquake chronology documented along the Denali fault system. Tentative correlations with very limited earthquake chronologies at along-fault paleoseismic sites do not provide unique prehistoric rupture length/location scenarios; however, forthcoming data from additional sites, incorporating new dating tools, and additional investigations at new

and existing sites will provide important constraints on past earthquake magnitude, location, and variability. In addition to the new constraints on paleoearthquake timing from the Dead Mouse site, our observations on surface-rupture properties and variability provide important parameters for the engineering of nearby railroad and highway projects, as well as proposed natural gas pipelines that would cross the Denali fault nearby. More data are required from other existing paleoseismic sites for a more comprehensive analysis of the spatial and temporal variability of Denali fault ruptures.

Data and Resources

All data used in this article and not generated by the authors came from published sources listed in the references and the following websites: Figure 1, https://lta.cr.usgs.gov/GTOPO30 (last accessed October 2016); Figure 2, https://lta.cr.usgs.gov/IFSAR_Alaska (last accessed October 2016).

Acknowledgments

Research supported by the U.S. Geological Survey (USGS), Department of the Interior, under USGS Award Number G14AP00134 to S. P. Bemis. The views and conclusions contained in this document are those of the authors and should not be interpreted as necessarily representing the official policies, either expressed or implied, of the U.S. Government. This article benefitted from comments by R. Koehler, an anonymous reviewer, and Associate Editor R. Briggs. Additional support for J. K. C., S. P. B., B. B., and T. P. T. from the University of Kentucky Department of Earth & Environmental Sciences. N. T. was supported by the SAC program from the College of Science and Health at Utah Valley University. Ahtna, Inc. generously permitted access to their land. J. DeVore, L. DeVore (Walker), S. Federschmidt, and J. Lepori provided additional field assistance. Radiocarbon analyses supported by National Science Foundation Award EAR 1250461 contributed to this study.

References

Bemis, S. P., S. Micklethwaite, D. Turner, M. R. James, S. Akciz, S. T. Thiele, and H. A. Bangash (2014). Ground-based and UAV-based photogrammetry: A multi-scale, high-resolution mapping tool for structural geology and paleoseismology, *J. Struct. Geol.* **69,** Part A, 163–178.

Bemis, S. P., R. J. Weldon, and G. A. Carver (2015). Slip partitioning along a continuously curved fault: Quaternary geologic controls on Denali fault system slip partitioning, growth of the Alaska Range, and the tectonics of south-central Alaska, *Lithosphere*, **7,** no. 3, 235–246.

Briner, J. P., and D. S. Kaufman (2008). Late Pleistocene mountain glaciation in Alaska: Key chronologies, *J. Quaternary Sci.* **23,** 659–670.

Bronk Ramsey, C. (2008). Deposition models for chronological records, *Quaternary Sci. Rev.* **27,** 42–60.

Bronk Ramsey, C. (2009). Bayesian analysis of radiocarbon dates, *Radiocarbon* **51,** 337–360.

Carver, G., G. Plafker, M. Metz, L. Cluff, B. Slemmons, E. Johnson, J. Roddick, and S. Sorensen (2004). Surface rupture on the Denali fault interpreted from tree damage during the 1912 Delta River M_w 7.2–7.4 earthquake: Implications for the 2002 Denali fault earthquake slip distribution, *Bull. Seismol. Soc. Am.* **94,** S58–S71.

Davies, L. J., B. J. L. Jensen, D. G. Froese, and K. L. Wallace (2016). Late Pleistocene and Holocene tephrostratigraphy of interior Alaska and Yukon: Key beds and chronologies over the past 30,000 years, *Quaternary Sci. Rev.* **146,** 28–53.

Dortch, J. M., L. A. Owen, M. W. Caffee, D. Li, and T. V. Lowell (2010). Beryllium-10 surface exposure dating of glacial successions in the Central Alaska Range, *J. Quaternary Sci.* **25,** 1259–1269.

Eberhart-Phillips, D., D. H. Christensen, T. M. Brocher, R. Hansen, N. A. Ruppert, P. J. Haeussler, and G. A. Abers (2006). Imaging the transition from Aleutian subduction to Yakutat collision in central Alaska, with local earthquakes and active source data, *J. Geophys. Res.* **111,** no. B11303, doi: 10.1029/2005JB004240.

Eberhart-Phillips, D., P. J. Haeussler, J. T. Freymueller, A. D. Frankel, C. M. Rubin, P. Craw, N. A. Ratchkovski, G. Anderson, G. A. Carver, A. J. Crone, *et al.* (2003). The 2002 Denali fault earthquake, Alaska: A large magnitude, slip-partitioned event, *Science* **300,** 1113–1119.

Freymueller, J. T., H. Woodard, S. C. Cohen, R. Cross, J. Elliott, C. F. Larsen, S. Hreinsdóttir, and C. Zweck (2008). Active deformation processes in Alaska, based on 15 years of GPS measurements, in *Active Tectonics and Seismic Potential of Alaska*, J. T. Freymueller, P. J. Haeussler, R. L. Wesson, and G. Ekström (Editors), American Geophysical Monograph 179, American Geophysical Union, Washington, D.C, 1–42.

Grantz, A. (1966). Strike-slip faults in Alaska, *U.S. Geol. Surv. Open-File Rept. 66-53*, 82 pp.

Haeussler, P. J. (2008). An overview of the neotectonics of interior Alaska: Far-field deformation from the Yakutat microplate collision, in *Active Tectonics and Seismic Potential of Alaska*, J. T. Freymueller, P. J. Haeussler, R. L. Wesson, and G. Ekström (Editors), American Geophysical Union Geophysical Monograph Series 179, American Geophysical Union, Washington, D.C., 83–108.

Haeussler, P. J. (2009). *Surface Rupture Map of the 2002 M 7.9 Denali Fault Earthquake, Alaska: Digital Data*, U.S. Geological Survey Data Series.

Haeussler, P. J., A. Matmon, D. P. Schwartz, G. Seitz, and A. J. Crone (2012). The Denali fault and interior Alaska tectonics in mid- to late-Cenozoic time, *Eos Trans. AGU* (Fall Meet), Abstract T14A–04.

Haeussler, P. J., D. P. Schwartz, T. E. Dawson, H. D. Stenner, J. J. Lienkaemper, B. Sherrod, F. R. Cinti, P. Montone, P. A. Craw, A. J. Crone, *et al.* (2004). Surface rupture and slip distribution of the Denali and Totschunda faults in the 3 November 2002 M 7.9 earthquake, Alaska, *Bull. Seismol. Soc. Am.* **94,** S23–S52.

Hamilton, T. D. (1994). Late Cenozoic glaciation of Alaska, in *The Geology of Alaska: Geology of North America*, G. Plafker and H. C. Berg (Editors), Vol. G-1, Geological Society of America, Boulder, Colorado, 813–844.

Hickman, R. G., K. W. Sherwood, and C. Craddock (1990). Structural evolution of the Early Tertiary Cantwell basin, south central Alaska, *Tectonics* **9,** 1433–1449.

Hubbard, T. D., R. D. Koehler, and R. A. Combellick (2011). High-resolution lidar data for Alaska infrastructure corridors, *Alaska Division of Geological & Geophysical Surveys Raw Data File 2011-3*, Alaska Division of Geological & Geophysical Surveys.

Keskinen, M., and J. Beget (2005). Age of most recent motion on the western Denali fault from Lichenometric dating of a large rockfall avalanche and offset moraines, *Eos Trans. AGU* (Fall Meet.), Abstract S13B–0189.

Koehler, R. D., R.-E. Farrell, P. A. C. Burns, and R. A. Combellick (2012). *Quaternary faults and folds in Alaska: A digital database* , Alaska Division of Geological & Geophysical Surveys Miscellaneous Publication, 141, doi: 10.14509/23944.

Koehler, R. D., S. F. Personius, D. P. Schwartz, P. J. Haeussler, and G. G. Seitz (2011). A Paleoseismic study along the central Denali fault, Chistochina Glacier area, south-central Alaska, *Report of Investigations*, Alaska Division of Geological & Geophysical Surveys.

Lienkaemper, J. J., and C. B. Ramsey (2009). OxCal: Versatile tool for developing paleoearthquake chronologies—A primer, *Seismol. Res. Lett.* **80,** 431–434.

Matmon, A., D. P. Schwartz, P. J. Haeussler, R. Finkel, J. J. Lienkaemper, H. D. Stenner, and T. Dawson (2006). Denali fault slip rates and Holocene-late Pleistocene kinematics of central Alaska, *Geology* **34,** 645–648.

Mériaux, A.-S., K. Sieh, R. C. Finkel, C. M. Rubin, M. H. Taylor, A. J. Meltzner, and F. J. Ryerson (2009). Kinematic behavior of southern Alaska constrained by westward decreasing postglacial slip rates on the Denali fault, Alaska, *J. Geophys. Res.* **114,** no. B03404, doi: 10.1029/2007JB005053.

Miller, M. L., D. C. Bradley, T. K. Bundtzen, and W. McClelland (2002). Late Cretaceous through Cenozoic strike-slip tectonics of southwestern Alaska, *J. Geol.* **110,** 247–270.

Nokleberg, W. J., D. J. Jones, and N. J. Silberling (1985). Origin and tectonic evolution of the Maclaren and Wrangellia terranes, eastern Alaska Range, Alaska, *Geol. Soc. Am. Bull.* **96,** 1251–1270.

Personius, S. F., A. J. Crone, P. A. C. Burns, and N. Rozell (2015). Paleoseismology of the Denali fault system at the Schist Creek site, central Alaska, *U.S. Geol. Surv. Open-File Rept. 2015-1225*, USGS Numbered Series, U.S. Geological Survey, Reston, Virginia.

Plafker, G., and H. C. Berg (1994). Overview of the geology and tectonic evolution of Alaska, in *The Geology of Alaska: Geology of North America*, G. Plafker and H. C. Berg (Editors), Vol. G-1, Geological Society of America, Boulder, Colorado, 989–1021.

Plafker, G., G. Carver, L. Cluff, and M. Metz (2006). Historic and paleoseismic evidence for non-characteristic earthquakes and the seismic cycle at the Delta River crossing of the Denali fault, Alaska, *Geol. Soc. Am. Abstr. Progr.* **38,** no. 5, 96.

Plafker, G., L. M. Gilpin, and J. C. Lahr (1994). Neotectonic map of Alaska, in *The Geology of Alaska*, G. Plafker and H. C. Berg (Editors), Vol. G-1, Geological Society of America, Geology of North America, Boulder, Colorado, plate 12, 1:2,500,000.

Reimer, P. J., E. Bard, A. Bayliss, J. W. Beck, P. G. Blackwell, C. B. Ramsey, C. E. Buck, H. Cheng, R. L. Edwards, M. Friedrich, *et al.* (2013). Intcal13 and Marine13 radiocarbon age calibration curves 0–50,000 years cal BP, *Radiocarbon* **55,** 1869–1887.

Reitman, N. G., S. E. K. Bennett, R. D. Gold, R. W. Briggs, and C. B. DuRoss (2015). High-resolution trench photomosaics from image-based modeling: Workflow and error analysis, *Bull. Seismol. Soc. Am.* **105,** no. 5, 2354–2366.

Ridgway, K. D., E. E. Thoms, P. W. Layer, M. E. Lesh, J. M. White, and S. V. Smith (2007). Neogene transpressional foreland basin development on the north side of the central Alaska Range, Usibelli Group and Nenana Gravel, Tanana basin, in *Tectonic Growth of a Collisional Continental Margin: Crustal Evolution of Southern Alaska*, K. D. Ridgway, J. M. Trop, J. M. G. Glen, and J. M. O'Neill (Editors), *Geol. Soc. Am. Spec. Pap.* 431**,** 507–547.

Ridgway, K. D., J. M. Trop, W. J. Nokleberg, C. M. Davidson, and K. R. Eastham (2002). Mesozoic and Cenozoic tectonics of the eastern and central Alaska Range: Progressive basin development and deformation in a suture zone, *Geol. Soc. Am. Bull.* **114,** 1480–1504.

Schwartz, D. P., P. J. Haeussler, A. Matmon, T. E. Dawson, G. Seitz, H. Stenner, S. Bemis, and E. Molhoek (2005). Earthquake geology of the Denali fault system, Alaska, *U.S. Geol. Surv. Open-File Rept. 2005-1131*, U. S. Geological Survey, Reston, Virginia, 25–29.

Schwartz, D. P., P. J. Haeussler, G. G. Seitz, and T. E. Dawson (2012). Why the 2002 Denali fault rupture propagated onto the Totschunda fault: Implications for fault branching and seismic hazards, *J. Geophys. Res.* **117,** no. B11304, doi: 10.1029/2011JB008918.

Seitz, G. J., P. J. Haeussler, A. J. Crone, P. Lipovsky, and D. P. Schwartz (2008). Eastern Denali fault slip rate and paleoseismic history, Kluane Lake Area, Yukon Territory, Canada, *Eos Trans. AGU* **89,** (Fall Meet. Suppl.), Abstract T53B–1947.

Strong, W. L., and G. H. L. Roi (1983). Root-system morphology of common boreal forest trees in Alberta, Canada, *Can. J. Forest Res.* **13,** 1164–1173.

Stuiver, M., and H. A. Polach (1977). Discussion: Reporting of ^{14}C data, *Radiocarbon* **19,** no. 3, 355–364.

Thoms, E. E. (2000). Late Cenozoic unroofing sequence and foreland basin development of the central Alaska Range: Implications from the Nenana Gravel, *M.S. Thesis*, University of Alaska Fairbanks, 221 pp.

Wallace, K., M. L. Coombs, L. A. Hayden, and C. F. Waythomas (2014). *Significance of a Near-Source Tephra-Stratigraphic Sequence to the Eruptive History of Hayes Volcano, South-Central Alaska*, U.S. Geological Survey.

Wesson, R. L., O. S. Boyd, C. S. Mueller, C. G. Bufe, A. D. Frankel, and M. D. Petersen (2007). Revision of time-independent probabilistic seismic hazard maps for Alaska, *U.S. Geol. Surv. Open-File Rept. 2007-1043*, USGS Numbered Series, U.S. Geological Survey.

Department of Earth & Environmental Sciences
University of Kentucky
101 Slone Research Building
Lexington, Kentucky 40506
sbemis@vt.edu
(J.K.C., S.P.B., T.P.T.)

Department of Earth Sciences
Utah Valley University
800 West University Parkway
Orem, Utah 84058
(N.T.)

Department of Geological Sciences
Brigham Young University
S389 Eyring Science Center
Provo, Utah 84602
(B.B.)

Manuscript received 3 March 2017;
Published Online 21 November 2017